Journal of
Materials Chemistry A

PAPER

View Article Online
View Journal | View Issue

Cite this: *J. Mater. Chem. A*, 2015, **3**, 16040

Poly(vinylidene fluoride) nanofibrous mats with covalently attached SiO_2 nanoparticles as an ionic liquid host: enhanced ion transport for electrochromic devices and lithium-ion batteries†

Rui Zhou,[a] Wanshuang Liu,[a] Xiayin Yao,[a] Yew Wei Leong[b] and Xuehong Lu*[a]

In this article, it is demonstrated that the electrospun poly(vinylidene fluoride-*co*-hexafluoropropylene) (P(VDF–HFP)) nanofibrous mat functionalized with (3-aminopropyl)triethoxysilane is a versatile platform for the fabrication of hybrid nanofibrous mats by covalently attaching various types of inorganic oxide nanoparticles on the nanofiber surface *via* a sol–gel process. In particular, SiO_2-on-P(VDF–HFP) nanofibrous mats synthesized using this method is an excellent ionic liquid (IL) host for electrolyte applications. The IL-based electrolytes in the form of free-standing mats are obtained by immersing SiO_2-on-P(VDF–HFP) mats in two types of liquid electrolytes, namely $LiClO_4$/1-butyl-3-methylimidazolium tetrafluoroborate and bis(trifluoromethane)sulfonimide lithium salt/1-butyl-1-methylpyrrolidinium bis(trifluoromethylsulfonyl)imide. It is found that the surface attached SiO_2 nanoparticles can effectively serve as salt dissociation promoters by interacting with the anions of both ILs and lithium salts through Lewis acid–base interactions. They dramatically enhance the ionic conductivity and lithium transference number of the electrolytes. In addition, better compatibility of the electrolytes with lithium electrodes is also observed in the presence of surface-attached SiO_2. Using IL-loaded SiO_2-on-P(VDF–HFP) nanofibrous mats as the electrolytes, electrochromic devices display higher transmittance contrast, while Li/$LiCoO_2$ batteries show significantly improved C-rate performance and cycling stability. This class of novel non-volatile electrolytes with high ionic conductivity also has the potential to be used in other electrochemical devices.

Received 24th March 2015
Accepted 25th June 2015

DOI: 10.1039/c5ta02154e

www.rsc.org/MaterialsA

1. Introduction

Room-temperature ionic liquids, a class of ionic materials having melting points lower than 25 °C, have attracted much attention over the past decade.[1,2] The development of ionic liquid (IL)-based electrolytes has been recognized as a viable solution to the safety problems faced by a range of electrochemical devices, including fuel cells, lithium ion batteries, supercapacitors and electrochromic devices.[3–7] The attractiveness of the ILs for use in electrolytes lies in their non-flammability and non-volatility as well as excellent electrochemical and thermal stability.[8] Meanwhile, ILs are frequently doped with lithium salts to compensate for their large ion size to further improve the device performance.[9] However, the potential problems caused by the liquid nature of the ILs, such as leakage, are considered as one of the critical factors limiting the long-term performance and practical use of the ILs. Thus, IL-based gel polymer electrolytes (GPEs), which consist of IL immobilized in a polymer matrix, are an attractive alternative to the IL-based liquid electrolytes.[10–13] Among many IL-based polymer electrolytes, IL-loaded electrospun mats have garnered increasing interest because in the mats there are interconnected pores between the randomly laid fibers, which facilitate electrolyte uptake and transport of ions.[14,15] Nevertheless, IL-loaded electrospun polymer mats also have some inherent limitations; namely, they have relatively weak mechanical strength, and their ionic conductivity and lithium-ion mobility are significantly lower than that of the traditional liquid electrolytes.

To address the aforementioned shortcomings of the IL-based polymer electrolytes, vigorous efforts have been undertaken, among which an effective approach is to incorporate inorganic fillers, such as SiO_2,[16] TiO_2 (ref. 17) and polyhedral oligomeric silsesquioxane (POSS)[18] into electrospun polymer nanofibers. It has been reported that these nanofillers can facilitate the dissociation of both ILs and lithium salts by Lewis acid–base interactions, giving enhanced ionic conductivity and lithium-ion mobility.[18–21] The addition of

---

[a] *School of Materials Science and Engineering, Nanyang Technological University, 50 Nanyang Avenue, Singapore 639798. E-mail: asxhlu@ntu.edu.sg*

[b] *Institute of Materials Research & Engineering, 3 Research Link, Singapore, 117602*

† Electronic supplementary information (ESI) available. See DOI: 10.1039/c5ta02154e

nanoparticles also leads to enhanced mechanical properties and compatibility with the lithium electrode.[22,23] Using this approach, the active fillers are, however, mainly embedded in the IL-swollen nanofibers and hence not directly accessible to liquid electrolytes in the pores, whereas the liquid phase is the major contributor to the overall ion transport properties.[24] Thus, a more appealing strategy is to attach inorganic nanoparticles on the surface of the nanofibers. This would allow the nanoparticles to have extensive Lewis acid–base interactions with the ionic species in the liquid electrolytes in the pores, and further improve the ionic conductivity and lithium electrode/electrolyte interfacial stability. Indeed, Yanilmaz *et al.* reported a method to produce SiO_2-on-poly(vinylidene fluoride) (PVDF) nanofibrous hybrid mats by combining electrospraying with electrospinning techniques, which allowed SiO_2 nanoparticles to be physically attached onto electrospun PVDF mats.[25] The obtained hybrid mats showed higher ionic conductivities, lower interfacial resistance with lithium electrodes and better C-rate performance in Li/$LiFeO_4$ batteries compared with those of neat PVDF mats.

In this article, for the first time, we report a novel approach to grow SiO_2 nanoparticles on the ethoxysilane-functionalized surface of electrospun poly(vinylidene fluoride-*co*-hexafluoropropylene) (P(VDF–HFP)) nanofibrous mats. This results in covalently attached SiO_2 nanoparticles uniformly distributed on the P(VDF–HFP) nanofiber surface (SiO_2-on-P(VDF–HFP)), preventing de-bonding at the fiber–nanoparticle interface during long-term cycling of electrochemical devices. To demonstrate the unique advantages of such novel organic–inorganic core–shell hybrid nanofibers, SiO_2-on-P(VDF–HFP) nanofibrous mats were used as the hosts for two types of ILs doped with lithium salts, namely $LiClO_4$/1-butyl-3-methylimidazolium tetrafluoroborate ($BMIM^+BF_4^-$) and bis(trifluoromethane)sulfonimide lithium (LiTFSI)/1-butyl-1-methylpyrrolidinium bis(trifluoromethylsulfonyl)imide ($PYR_{14}^+TFSI^-$). The former was applied in electrochromic devices, while the latter was employed in lithium-ion batteries. Herein, we demonstrate that with an optimized SiO_2 content, the mechanical strength, ionic conductivity and lithium transport properties of the electrolytes all exhibit substantial enhancements, and both the electrochromic device and lithium ion battery show significantly improved performance. Furthermore, the synthesis method presented here is generic. The ethoxysilane groups grafted on the nanofiber surface can also facilitate the growth of many other types of oxide nanoparticles such as Al_2O_3, ZnO and TiO_2 *via* a sol–gel process, and the obtained hybrid materials may be used for a wide variety of applications.

2. Experimental

2.1. Materials

$LiClO_4$, $BMIM^+BF_4^-$, LiTFSI, $PYR_{14}^+TFSI^-$, 1,3-diaminopropane, (3-aminopropyl)triethoxysilane (APTES), tetraethoxysilane (TEOS), aniline, 4-dodecylbenzene sulfonic acid (DBSA), titanium butoxide, xylene, *N*,*N*-dimethylformamide (DMF), ethanol and acetone were obtained from Sigma-Aldrich Corporation (USA). $LiClO_4$ was dried in a vacuum at 100 °C for 24 h prior to use. P(VDF–HFP) powder (solef 11008, M_w = 115 000) was purchased from Solvay Solexis Inc. (USA) and used as received. A DBSA-doped polyaniline (PANI)–TiO_2 hybrid was prepared *via* a sol–gel process involving the reaction of titanium butoxide and a hybrid bridging compound, followed by oxidative emulsion copolymerization of aniline in the presence of the hybrid gel and DBSA.[26] Conducting indium tin oxide (ITO) glass ($5–15\ \Omega\ \square^{-1}$) was purchased from Delta Technologies Co. (USA) and cleaned by ultrasonication in a series of solvents including detergent, deionized water and acetone for 10 min each prior to use.

2.2. Preparation of SiO_2-on-P(VDF–HFP) nanofibrous electrospun mats

Chemically cross-linked electrospun P(VDF–HFP) mats with 1 wt% 1,3-diaminopropane were prepared according to our previous publication.[6] A two-step method was adopted to attach SiO_2 nanoparticles on the surface of the P(VDF–HFP) nanofibers. In the first step, silane groups were grafted onto the fiber surface by immersing the electrospun mats in 5 wt% APTES ethanol solution at 70 °C for 1, 3, 5 and 10 h. The product obtained was denoted as silane-on-P(VDF–HFP). In the second step, the silane-on-P(VDF–HFP) nanofibrous electrospun mats were transferred into TEOS, DI water and ethanol solution with a molar ratio of 1 : 3 : 8.5 under vigorous shaking. NH_4OH was added dropwise to achieve a final pH value of 11. The above process was conducted for 0.5, 1, 3, 5 and 10 h, respectively, to achieve different SiO_2 contents. After thoroughly washing with ethanol and deionized water, the SiO_2-attached electrospun mats were dried at 60 °C under vacuum. The product obtained was denoted as SiO_2-on-P(VDF–HFP). The SiO_2 contents in the final mats were calculated based on the weights of the electrospun mats before and after SiO_2 attachment.

2.3. Preparation of IL-based polymer and hybrid electrolytes

The IL-based electrolytes were obtained by soaking the electrospun mats with and without SiO_2 in $BMIM^+BF_4^-$, and 1 mol kg^{-1} $LiClO_4/BMIM^+BF_4^-$ solutions for 12 h at 60 °C, respectively. The mats were then placed onto a piece of cellulose paper and pressed with a 20 g weight to absorb the excess IL. The electrolyte uptake (ε) was calculated using eqn (1)

$$\varepsilon(\%) = \frac{M - M_0}{M_0} \times 100 \tag{1}$$

where M_0 is the mass of dry electrospun mats and M is the mass after soaking with IL electrolytes.

2.4. Characterization

The Raman spectra of the electrospun mats were recorded using a Witec confocal Raman spectrometer with an excitation light of 488 nm. Fourier transform infrared (FTIR) spectra were obtained using the attenuated total reflection (ATR) attachment on a Perkin Elmer Spectrum GX FTIR spectrometer with a wave number range of 600 to 4000 cm^{-1}. Wide angle X-ray diffraction (WAXD) patterns of the electrospun mats were recorded on a Bruker GADDS X-ray diffractometer using Cu Kα radiation (λ = 0.154 nm) generated at 40 kV and 40 mA. The morphologies of the electrospun nanofibrous mats were investigated using a field-emission scanning electron microscope (FESEM, JEOL 7600F). Tensile tests were performed on an Instron Tester 5567 with a 500 N load cell at a crosshead speed of 5 mm min^{-1}. Dumb-bell-shaped specimens were prepared according to the ASTM D638 standard with dimensions of 25 mm × 3.2 mm × 0.1 mm. Each reported value was the average of five specimens.

The ionic conductivities were determined by AC impedance spectroscopy using an Autolab PGSTAT30 electrochemical workstation. IL-loaded electrospun mats were sandwiched between two polished stainless steel electrodes, and the spectra were obtained over a frequency range from 10^5 Hz to 10 Hz with AC amplitude of 10 mV. Lithium transference numbers (T_{Li^+}) were measured using the method of chronoamperometry in the Li/electrolyte/Li cells with a polarization voltage of 30 mV (ΔV) according to our previous publication.[18] In brief, the initial current, I_0, and the steady-state current, I_{ss}, that flowed through the cell were measured. The same cell was also monitored by impedance spectroscopy in the frequency range of 10^6 to 10^{-1} Hz to obtain the initial, R_0, and the steady-state, R_{ss}, Li/electrolyte resistance. The lithium transference numbers (T_{Li^+}) were calculated by eqn (2)

$$T_{\text{Li}^+} = \frac{I_{\text{ss}}(\Delta V - R_0 I_0)}{I_0(\Delta V - R_{\text{ss}} I_{\text{ss}})} \tag{2}$$

The interface resistance (R_{int}) between the IL-loaded electrospun mats and the lithium-metal electrode was examined using the impedance response of the Li/electrolyte/Li cells.

2.5. Fabrication and testing of electrochromic devices

PANI–TiO_2 emulsion in xylene was spin-coated onto cleaned ITO-coated glass to form a thin film. Single-active-layer electrochromic devices with the configuration of ITO glass/electrochromic layer (PANI–TiO_2)/electrolyte/ITO glass were fabricated. The visible transmittance spectra and switching kinetics of the devices were recorded on a UV-vis spectrophotometer (Shimadzu UV-2501 PC), by applying constant potentials and square-wave potentials using the Autolab PGSTAT 302 potentiostat/galvanostat analyzer. The switching kinetics of the devices was determined at the wavelength of 650 nm (λ_{max}), at which the maximum transmittance contrast was achieved under the constant potentials. For dynamic switching, the potential was stepped between −2.0 V and +2.0 V with a step interval of 40 s.[27]

2.6. Assembly and testing of lithium-ion battery cathodes

A standard CR2032 coin cell with lithium metal as the counter electrode was used for testing the electrochemical properties of the cathode. The working electrode was prepared by spreading a mixture of LiCoO_2 (80 wt%), Super-P (10 wt%) and PVDF (10 wt%) dispersed in *N*-methyl pyrrolidone (NMP) onto an aluminium foil current collector. IL-based electrolytes were prepared by soaking a commercial Celgard 2325 membrane, neat P(VDF–HFP) and SiO_2 (15.4 wt%)-on-P(VDF–HFP) nanofibrous electrospun mats in 0.3 mol kg^{-1} LiTFSI/$\text{PYR}_{14}{}^+\text{TFSI}^-$ for 24 h in an argon filled glovebox. Electrochemical tests were performed on a NEWARE-CT3008 battery test system (Neware Technology Limited, Shenzhen, China). The cells were cycled between 2.8 and 4.2 V *vs.* Li^+/Li.

3. Results and discussion

3.1. Structures and morphologies of the SiO_2-on-P(VDF–HFP) nanofibrous electrospun mats

Scheme 1 shows the route for the preparation of SiO_2-on-P(VDF–HFP) nanofibrous electrospun mats. To grow SiO_2 nanoparticles on the P(VDF–HFP) nanofiber surface, the fibers were first treated with an amine-terminated silane (APTES). Owing to the strong polarity of the C–F bond, nucleophiles such as amines, phenols and thiolene are effective reagents for the introduction of functional groups onto fluoropolymer main chains.[28] As shown in Scheme 1, the reaction with APTES creates a C═N double bond, leading to covalent tethering of APTES onto P(VDF–HFP). Raman spectra are used to verify the reaction. As illustrated in Fig. 1a, neat P(VDF–HFP) has no Raman signal in the range of 2000–1000 cm^{-1}.[29] By contrast, new bands corresponding to C═N and C–N stretching vibrations appear at 1541 and 1141 cm^{-1} after silane attachment, signifying the covalent tethering of APTES on the surface of the nanofibers. Fig. 1b shows the FTIR spectra of P(VDF–HFP), silane-on-P(VDF–HFP) and SiO_2-on-P(VDF–HFP) nanofibrous mats. The absorption band at 1640 cm^{-1} for both silane-on-P(VDF–HFP) and SiO_2-on-P(VDF–HFP) can be attributed to the C═N stretching vibration, which is in accordance with the Raman spectra. In addition, by comparing the spectra of P(VDF–HFP) before and after modification, the intensity of the broad band centred at 1070 cm^{-1} clearly increases for SiO_2-on-P(VDF–HFP) (using the C–F symmetric stretching band at 879 cm^{-1} as reference). This is due to the overlap of the band from the F–C–F symmetric stretching vibration (at 1072 cm^{-1})[30] and the band from the Si–O–Si antisymmetric stretching vibration (at 1070 cm^{-1}),[31] indicating the successful attachment of SiO_2 on the fiber surface. WAXD studies were also performed to investigate the structures of the hybrid mats. As illustrated in Fig. S1,† no diffraction peak corresponding to the crystalline SiO_2 phase is observed for all the hybrid mats, indicating the amorphous nature of the attached SiO_2 nanoparticles.

Fig. 2a shows that with the attachment of SiO_2 nanoparticles, the nanofibrous mats retain their flexibility. FESEM studies indicate that the attachment of SiO_2 does not block the interpenetrating pores of the mats (Fig. 2b). Most SiO_2 nanoparticles have a size of 10–20 nm, while the slightly larger ones are likely to be the aggregates of the smaller ones as they have irregular shapes. These nanoparticles are uniformly distributed on the fiber surface (Fig. 2c–e). By contrast, without the APTES treatment, a relatively smooth fiber surface (Fig. S2a†) is observed for the neat P(VDF–HFP) electrospun mats after the sol–gel process, and the FTIR spectrum shows no SiO_2 signal (Fig. S2b†). The combination of FESEM and FTIR studies confirms that the attachment of APTES on the fiber surface is an indispensable step to effectively grow covalently bonded SiO_2 nanoparticles on the fiber surface. Cross-sectional SEM micrographs of the

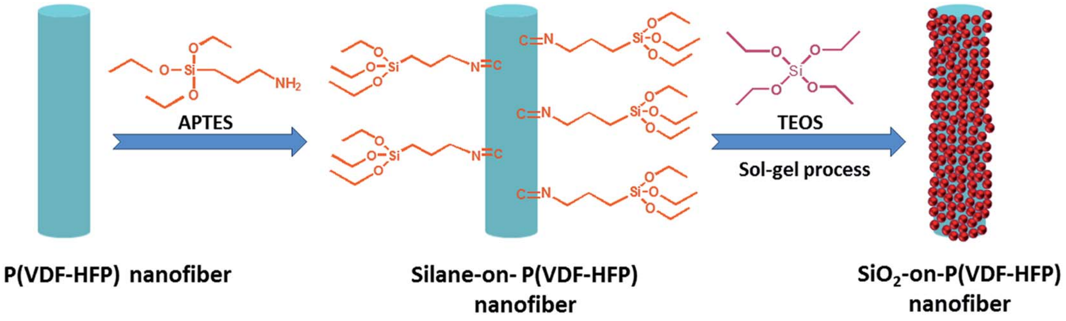

Scheme 1 The schematic showing the preparation route of SiO_2-on-P(VDF–HFP) nanofibrous electrospun mats.

hybrid nanofibers are provided in Fig. S3.† It shows that the thickness of the SiO_2 layer on the P(VDF–HFP) nanofiber surface is approximately 10–20 nm. More FESEM images of the SiO_2-on-P(VDF–HFP) mats with different SiO_2 contents are provided in Fig. S4.† The SiO_2 contents in the hybrid mats for different silane (APTES) grafting times and sol–gel processing times are also presented in Fig. S5.†

3.2. Mechanical properties of the SiO_2-on-P(VDF–HFP) nanofibrous electrospun mats

Since the hybrid electrolytes must withstand the forces applied during device fabrication and cycling stress, their mechanical properties are important parameters in determining their long-term performance. The apparent Young's modulus and tensile strength of SiO_2-on-P(VDF–HFP) nanofibrous mats with different SiO_2 contents are shown in Fig. 3. Both apparent Young's modulus and ultimate tensile strength show a sharp increase at the SiO_2 content of 12.6 wt%, which is presumably due to the load transfer from the polymer fibers to inter-connected SiO_2 nanoparticles. The apparent tensile strength decreases with further increase of the SiO_2 content, which can be explained by the increased brittleness, causing a decrease in the strain at break. It is worth noting that at similar SiO_2 loadings, the apparent modulus values of the SiO_2-on-P(VDF–HFP) mats are significantly higher than that of the hybrid mats prepared by simply incorporating SiO_2 nanoparticles into polymer nanofibers.[16,32,33]

3.3. Effects of SiO_2 on ionic conductivity and salt dissociation

Table 1 summarizes the electrolyte uptake and ionic conductivity of SiO_2-on-P(VDF–HFP) nanofibrous mats after loading with $BMIM^+BF_4^-$ and $LiClO_4/BMIM^+BF_4^-$. The electrolyte uptake is due to swelling of the polymer and filling the pores of the mats by the ILs. For the SiO_2-on-P(VDF–HFP) nanofibrous mats loaded with neat IL, both the electrolyte uptake and ionic conductivity increase with the SiO_2 content up to 1.4 wt%, followed by a drop. The increased electrolyte uptake can be attributed to the large surface area and hydrophilic nature of SiO_2 nanoparticles, which help to trap more liquid electrolyte. The subsequent decrease of the electrolyte uptake can be explained by the decreased porosity resulting from larger fiber diameters. The highest ionic conductivity of 7.8 mS cm^{-1} is achieved at 1.4 wt% SiO_2 content, which is much higher than that of neat $BMIM^+BF_4^-$ (3.5 mS cm^{-1}).[34] The –OH groups on the SiO_2 surfaces can act as Lewis acid centres, interacting with the anions (BF_4^-) of the IL through Lewis acid–base interactions, and hence leading to enhanced dissociation of the IL and more free ions. The combination of the increased electrolyte uptake and increased number of free ions leads to a significant improvement of ionic conductivity.

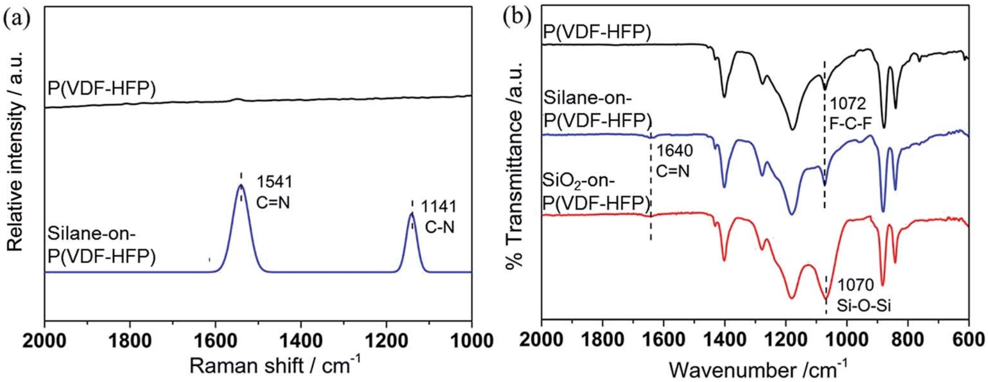

Fig. 1 (a) Raman spectra of P(VDF–HFP) and silane-on-P(VDF–HFP) nanofibrous electrospun mats; (b) FTIR spectra of P(VDF–HFP), silane-on-P(VDF–HFP) and SiO_2-on-P(VDF–HFP) nanofibrous electrospun mats.

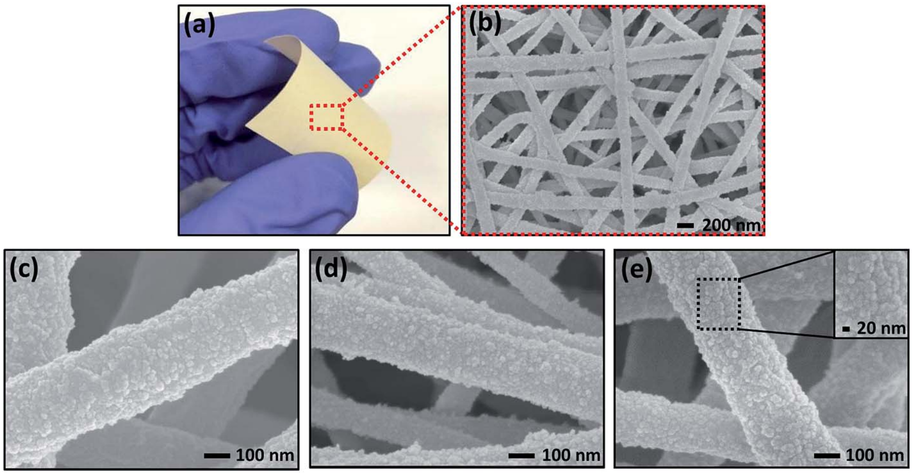

Fig. 2 (a) Photograph of the SiO_2-on-P(VDF–HFP) nanofibrous electrospun mats and (b) the corresponding SEM image at low magnification; SEM images of the hybrid mats with (c) 1.4 wt%, (d) 8.6 wt% and (e) 15.4 wt% SiO_2 at high magnification with an enlarged inset.

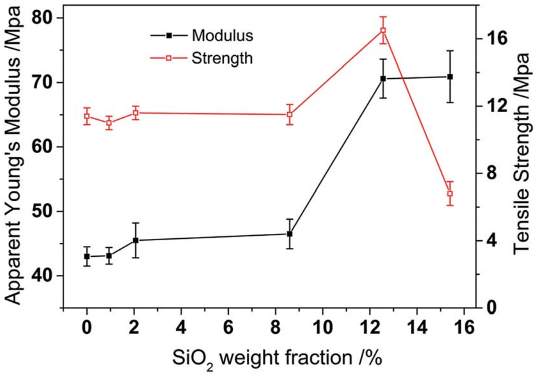

Fig. 3 The apparent Young's modulus and tensile strength of the SiO_2-on-P(VDF–HFP) nanofibrous mats with different SiO_2 contents.

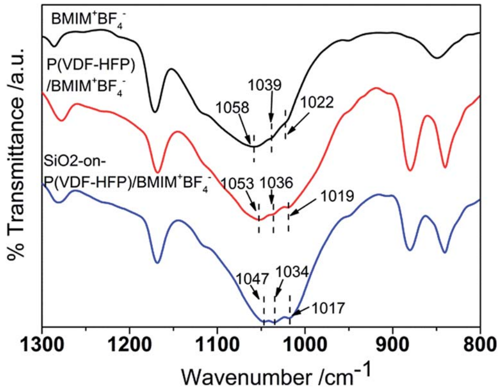

Fig. 4 FTIR spectra of neat $BMIM^+BF_4^-$, P(VDF–HFP) and SiO_2 (15.4 wt%)-on-P(VDF–HFP) nanofibrous electrospun mats after loading with $BMIM^+BF_4^-$.

FTIR spectroscopy is used to verify the interactions between BF_4^- and –OH groups on the SiO_2 surfaces. As shown in Fig. 4, the triplet bands at 1058, 1039 and 1022 cm^{-1} in neat $BMIM^+BF_4^-$ are ascribed to the antisymmetric B–F stretching vibration.[35] The triplet bands shift to lower frequencies for the IL-loaded electrospun P(VDF–HFP) mats, which is presumably caused by the complexation of the polymer backbone with the IL. Moreover, it is clearly visible that the triplet bands further shift to 1047, 1034 and 1017 cm^{-1} for the IL-loaded electrospun mats with SiO_2. A lower wavenumber indicates stronger interactions, signifying the formation of Lewis acid–base interactions between hydroxyl groups of SiO_2 and BF_4^- anions.

Table 1 Electrolyte uptake and ionic conductivity of SiO_2-on-P(VDF–HFP) nanofibrous mats with different SiO_2 contents (measured at 20 °C)

	$BMIM^+BF_4^-$		$LiClO_4/BMIM^+BF_4^-$ (1 mol kg^{-1})	
SiO_2 content	Electrolyte uptake (%)	Ionic conductivity (mS cm^{-1})	Electrolyte uptake (%)	Ionic conductivity (mS cm^{-1})
0 wt%	440	2.6 ± 0.2	460	2.3 ± 0.1
0.9 wt%	440	6.5 ± 0.3	460	4.3 ± 0.1
1.1 wt%	450	6.6 ± 0.3	480	4.5 ± 0.2
1.4 wt%	500	7.8 ± 0.4	510	4.8 ± 0.2
2.1 wt%	420	5.6 ± 0.2	400	6.2 ± 0.3
8.6 wt%	360	5.6 ± 0.2	320	6.2 ± 0.2
12.6 wt%	330	5.4 ± 0.1	310	6.5 ± 0.2
15.4 wt%	300	5.2 ± 0.2	290	8.6 ± 0.2

These favourable interactions promote the dissociation of the IL, and result in improved ionic conductivity as demonstrated earlier.

In order to address the low ion mobility issue caused by the large cation size of the ILs, $LiClO_4$ was introduced into $BMIM^+BF_4^-$. The electrolyte uptake of SiO_2-on-P(VDF–HFP) nanofibrous electrospun mats shows the same trend as those loaded with neat $BMIM^+BF_4^-$, whereas the ionic conductivity monotonically increases with the SiO_2 content. The mat with 15.4 wt% SiO_2 exhibits the highest ionic conductivity of 8.6 mS cm^{-1}, which is comparable to that of traditional organic solvent-based electrolytes.[16] For the mats with 1.4 wt% and lower SiO_2 content, the introduction of $LiClO_4$ into $BMIM^+BF_4^-$ leads to a slight decrease in conductivity. This is due to the formation of stiffer ionic aggregates, provoking an increase in viscosity and a diminution in the self-diffusion coefficients and conductivity.[36] For the mats with a higher SiO_2 content, the conductivity increases with the incorporation of $LiClO_4$. The enhanced conductivity at higher SiO_2 content is due to increased salt dissociation, as the larger amounts of hydroxyl groups effectively interact with both types of anions (ClO_4^- and BF_4^-), breaking the interactions between the ion pairs and boosting the concentration of free conducting ions. Additionally, the addition of the lithium salt increases charge density, and hence requires more active functional groups to effectively interact with them, which explains the monotonic increase of conductivity with the SiO_2 content. The above results demonstrate that the surface-tethered SiO_2 is very effective in improving the ionic conductivity of the IL-based electrolytes.

To obtain direct evidence for the interactions between ClO_4^- and –OH groups on the SiO_2 surfaces, Raman spectroscopy is conducted. As shown in Fig. 5, a band at 934 cm^{-1} is accompanied by a shoulder on the high frequency side (942 cm^{-1}), which are attributed to the symmetric stretching vibration of ClO_4^-. The former arises from free ClO_4^- anions, while the latter originates from contact-ion pairs or the ClO_4^- anions bound with the –OH group of SiO_2.[37] The intensity of the shoulder peak at 942 cm^{-1} clearly increases after the incorporation of SiO_2. The increase in the high frequency component reveals that the –OH groups on SiO_2 surfaces function as Lewis acidic centres, interacting with ClO_4^- anions through Lewis acid–base interactions. The interaction of ClO_4^- anions with SiO_2 promotes the dissociation of $LiClO_4$ and thus frees up Li^+ ions.

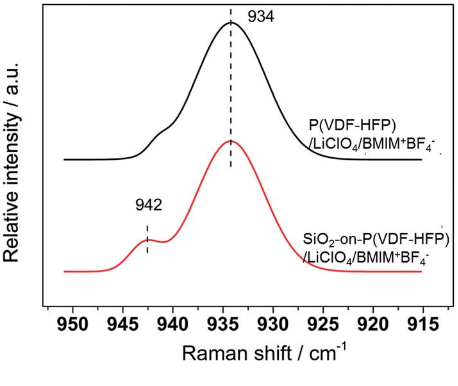

Fig. 5 Raman spectra of P(VDF–HFP) and SiO_2 (15.4 wt%)-on-P(VDF–HFP) nanofibrous electrospun mats loaded with $LiClO_4/BMIM^+BF_4^-$.

To confirm the effect of SiO_2 on the migration of Li^+ ions in the electrolytes, their lithium transference numbers (T_{Li^+}) were measured using the DC polarization method combined with impedance techniques. Fig. 6 shows the current–time data and impedance spectra of $LiClO_4/BMIM^+BF_4^-$ loaded in neat P(VDF–HFP) and SiO_2 (15.4 wt%)-on-P(VDF–HFP) mats. The current flowing through the cell drops sharply within a few minutes, and then decreases gradually with time. The resistance of the Li/electrolyte interface is obtained from the impedance spectra, and T_{Li^+} values are calculated using eqn (2). With the incorporation of SiO_2, the T_{Li^+} value increases from 0.25 to 0.41, which is due to the improved lithium salt dissociation as discussed above. However, this increase is not as significant as that of the ionic conductivity because the hydroxyl groups interact with both types of anions (ClO_4^- and BF_4^-), facilitating the transport of both $BMIM^+$ and Li^+ cations. Thus $BMIM^+$ transference number may also increase, affecting the degree of enhancement in the T_{Li^+} value.

3.4. Performance of the electrolytes in electrochromic devices

Electrochromic devices have found a wide range of applications including smart windows and display panels owing to their energy-saving potential. However, the problems associated with solvent volatility and electrolyte leakage would cause safety concerns and lead to poor long-term durability.[38] Thereby, to make electrochromic devices safer and more durable, the choice of the electrolyte is crucial. IL-based electrolytes stand out in this regard due to their unique advantages. Additionally, in order to fabricate electrochromic devices capable of delivering higher optical contrast, lithium salt is commonly introduced into IL-based electrolytes, which greatly facilitates the doping and dedoping process of the electrochromic layer due to its much smaller ion size.[9] To demonstrate the effects of attaching SiO_2 on P(VDF–HFP) on the performance of the IL-based electrolytes, devices using P(VDF–HFP)/$LiClO_4/BMIM^+BF_4^-$ and SiO_2 (15.4 wt%)-on-P(VDF–HFP)/$LiClO_4/BMIM^+BF_4^-$ as electrolytes were fabricated and tested under the same conditions. Fig. 7 shows the switching behaviours of the devices under the applied step potential between +2.0 V and −2.0 V at the wavelength of 650 nm (λ_{max}, at which the maximum transmittance contrast was achieved under constant potentials). The device with the SiO_2-on-P(VDF–HFP)/$LiClO_4/BMIM^+BF_4^-$ electrolyte exhibits a transmittance contrast of 72%, which is 20% higher than that with P(VDF–HFP)/$LiClO_4/BMIM^+BF_4^-$. The higher contrast achieved may be attributed to the increased number of free ions, especially Li^+ ions. Consequently, more ions can easily diffuse into the active layer and more active units can be effectively switched.

3.5. Performance of the electrolytes in lithium-ion batteries

IL-based electrolytes are presently considered as promising materials with great potential for a variety of electrochemical devices, among which lithium-ion battery is one of the most

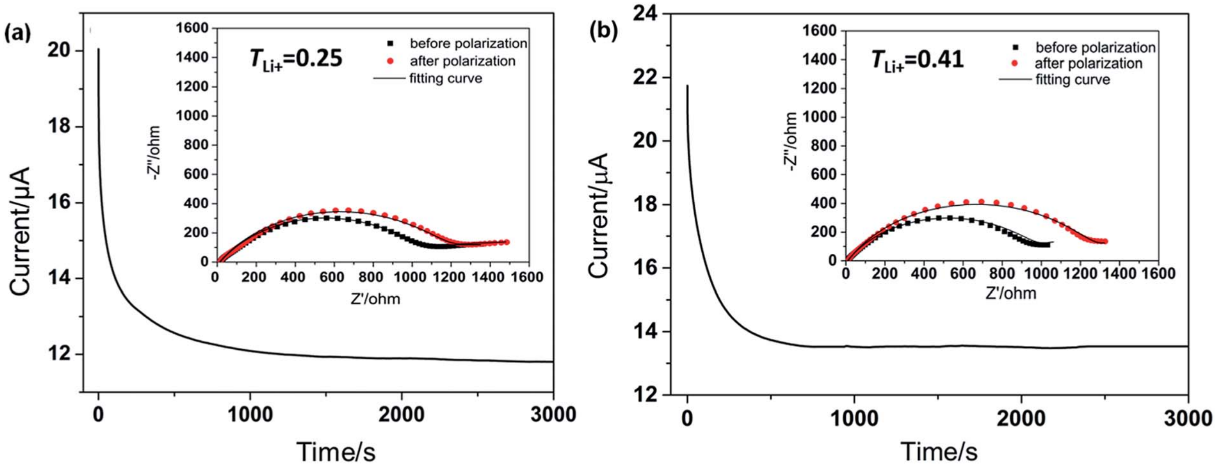

Fig. 6 Chronoamperometric curves of Li/electrolyte/Li symmetric cells with P(VDF–HFP) and SiO_2 (15.4 wt%)-on-P(VDF–HFP) nanofibrous mats loaded with $LiClO_4/BMIM^+BF_4^-$ as electrolytes, at 30 mV DC. The insets show the impedance response of the same cell before and after the DC polarization.

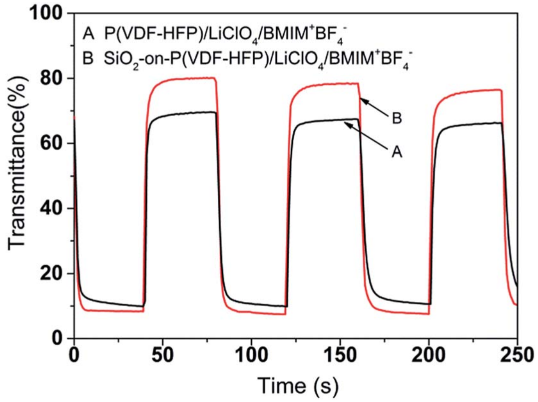

Fig. 7 Switching curves of PANI–TiO_2-based single-layer electrochromic devices with P(VDF–HFP)/$LiClO_4/BMIM^+BF_4^-$ and SiO_2 (15.4 wt%)-on-P(VDF–HFP)/$LiClO_4/BMIM^+BF_4^-$ as electrolytes under square-wave potentials oscillating between +2.0 V and −2.0 V.

challenging application areas. Despite the unique advantages of the IL-based electrolytes, their rather low Li^+ ion conductivity due to the relatively high viscosity and ion complexes formed among ions may cause a concentration gradient within the battery and deteriorate the battery performance under high current density.[39] To demonstrate the effectiveness of the P(VDF–HFP) electrospun mats tethered with SiO_2 nanoparticles in improving Li^+ transport properties, three IL hosts were evaluated, namely a commercial Celgard membrane, neat P(VDF–HFP) and SiO_2 (15.4 wt%)-on-P(VDF–HFP) nanofibrous mats, which were all loaded with 0.3 mol kg^{-1} $LiTFSI/PYR_{14}^{+-}$ $TFSI^-$ to provide high ionic conductivity, wide electrochemical window and good compatibility toward the lithium electrode. The T_{Li^+} values of the Celgard membrane, neat P(VDF–HFP) and SiO_2 (15.4 wt%)-on-P(VDF–HFP) nanofibrous mats are 0.23, 0.31 and 0.68, respectively. In comparison with the Celgard membrane, the T_{Li^+} value of P(VDF–HFP) electrospun mats shows a slight increase. This indicates that P(VDF–HFP) polymer chains can solvate anions ($TFSI^-$) and hinder their motions to some extent. It is striking to see that with the attachment of SiO_2 on the fiber surface, the T_{Li^+} value increases drastically. This is attributed to the interactions between the Lewis acid sites on SiO_2 and $TFSI^-$ anions that impede the formation of ionic complexes and release more free Li^+. A high T_{Li^+} value would decrease the electrolyte polarization caused by anion accumulation and suppresses the concentration gradient to facilitate lithium-ion transport, which is beneficial for the rate performance of lithium-ion batteries.

The chemical stabilities of these IL electrolytes against the lithium anode are important for the cycle life, power density and safety of lithium-ion batteries, which can be characterized by the interfacial resistance between the electrolytes and the lithium electrode. The interfacial resistance is associated with the passivation layer on the lithium electrode and the associated charge transfer resistances, which can be investigated by the electrochemical impedance spectra (EIS) using the Li/electrolyte/Li symmetric cells. Due to the low electrochemical potential of lithium metal, the electrolyte undergoes reduction on its surface, leading to the growing of an electronically insulating but ionically conducting solid electrolyte interphase (SEI) on the anode surface.[40] The passivating SEI layer can protect the electrode from further reaction with the electrolyte, thereby limiting the degradation of the electrolyte, whereas also leads to irreversible capacity loss since the SEI layer contains lithium compounds.[41,42] Therefore, a thin and stable SEI layer is essential for achieving high-performance lithium-ion batteries. As shown in Fig. 8a, for the three $LiTFSI/PYR_{14}^+TFSI^-$-loaded membranes, the interfacial resistance increases initially, and then a dynamic equilibrium state is achieved. The increase in the interfacial resistance with the storage time may be associated with the growth of the passivation layer on the lithium electrode surface and degradation of the direct physical contact between the electrode and the membrane. For membranes without nanoparticles, the stabilization takes a few days. Whereas, P(VDF–HFP) electrospun mats exhibit lower interfacial resistance compared with the commercial Celgard membrane. This can be attributed to a larger porosity, higher electrolyte uptake, and better electrolyte/lithium electrode affinity of the P(VDF–HFP) mats, which facilitate the migration of Li^+ at the electrolyte/electrode interface and cause a decrease in the interfacial resistance.[14] The introduction of covalently bonded SiO_2 nanoparticles onto the P(VDF–HFP) nanofibrous mats further reduces the interfacial resistance. There is only a very small initial surge in the first few hours and the resistance remains almost constant afterwards. This suggests that the presence of SiO_2 nanoparticles may lead to a thinner and more stable SEI.[25] The SiO_2 nanoparticles, which have large surface area and high hydrophilicity, can effectively hold the liquid electrolyte by capillary force and help to trap residual trace of moistures and impurities. This would inhibit the reactions of the electrolyte and impurities with the lithium metal, resulting in smaller and more stable interfacial resistance.[25]

In order to evaluate the effectiveness of the SiO_2 (15.4 wt%)-on-P(VDF–HFP) nanofibrous mats in improving the rate performance of lithium-ion batteries, Li/$LiCoO_2$ cells using this membrane loaded with 0.3 mol kg^{-1} LiTFSI/$PYR_{14}{}^+TFSI^-$ as electrolytes were fabricated and tested. For comparison, cells using the commercial Celgard membrane and neat P(VDF–HFP) mat loaded with the same amount of LiTFSI/$PYR_{14}{}^+TFSI^-$ were also tested. Fig. 8b shows the discharge C-rate capabilities of the Li/$LiCoO_2$ cells containing the aforementioned three electrolyte systems. It is clear that the SiO_2 (15.4 wt%)-on-P(VDF–HFP) nanofibrous mat exhibits the highest discharge capacity at each C-rate, and the differences become larger at higher current density where the influence of Li^+ ion conductivity is more significant. The notable improvement in the rate performance of Li-ion batteries can be attributed to the unique advantages of this novel SiO_2-on-P(VDF–HFP) nanofibrous mat, which provides a higher T_{Li^+} value, and better compatibility with the lithium electrode as demonstrated above. The discharge capacities at 0.5C as a function of cycle number of the three systems are also compared, and the results are shown in Fig. 8c. It is observed that the cell based on the SiO_2 (15.4 wt%)-on-P(VDF–HFP) nanofibrous mat delivers a high initial discharge capacity of 121 mA h g^{-1}, and shows a capacity retention of 95% after the 50th cycle. The superior cyclability of the SiO_2 (15.4 wt%)-on-P(VDF–HFP) nanofibrous mat is associated with its high Li^+ ion conductivity and better compatibility with the lithium electrode.

3.6. Covalently attaching metal oxide nanoparticles on polymer nanofibers

Herein we report that ethoxysilane groups grafted on the P(VDF–HFP) nanofiber surface can also facilitate the covalent

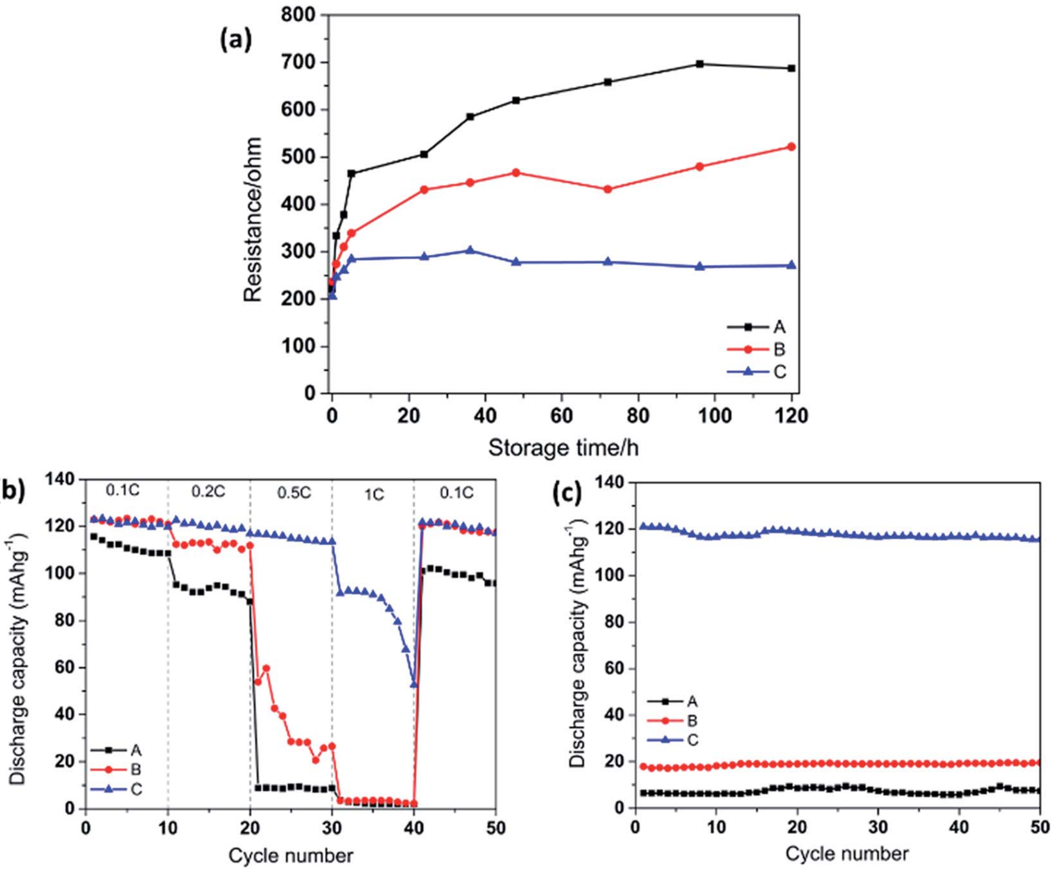

Fig. 8 (a) Time dependence of the electrolyte/lithium electrode interfacial resistance at room temperature; (b) rate discharge capacity of Li/$LiCoO_2$ cells under difference current density; (c) cycling stability at 0.5C (A, B and –C represent the commercial Celgard membrane, P(VDF–HFP) and SiO_2 (15.4 wt%)-on-P(VDF–HFP) nanofibrous electrospun mats after loading with 0.3 mol kg^{-1} LiTFSI/$PYR_{14}{}^+TFSI^-$).

attachment of metal oxide nanoparticles *via* a sol–gel process. Fig. S6† shows the SEM images of APTES-modified P(VDF–HFP) mats after treatment with TiO_2 and Al_2O_3 precursor solutions. It is clear that both TiO_2 and Al_2O_3 nanoparticles have been successfully attached on the nanofiber surface. This demonstrates that the ethoxysilane-functionalized P(VDF–HFP) nanofibrous mats are a versatile platform for the synthesis of a wide variety of hybrid nanofibrous mats with metal oxide nanoparticles covalently attached on the nanofiber surface.

Both TiO_2 and Al_2O_3 attached P(VDF–HFP) electrospun mats were loaded with $BMIM^+BF_4^-$, and their corresponding ionic conductivities are listed in Table S1.† This shows that the incorporation of both TiO_2 and Al_2O_3 nanoparticles leads to a higher ionic conductivity compared with that of the neat P(VDF–HFP) mat, whereas the extent of the increase is smaller than that obtained by the attachment of the same amount of SiO_2. This may be explained by the stronger Lewis acidity of SiO_2 nanoparticles, which may interact with BF_4^- anions more strongly, hence releasing more $BMIM^+$ cations. Nevertheless, it is believed that TiO_2-on-P(VDF–HFP), Al_2O_3-on-P(VDF–HFP) and other metal oxide-on-P(VDF–HFP) nanofibrous mats that may be synthesized using this method may find a wide range of applications in areas such as filtration, UV protection and environmental applications.

4. Conclusion

SiO_2-on-P(VDF–HFP) nanofibrous mats have been successfully prepared by a combination surface functionalization of electrospun mats and a sol–gel protocol. SiO_2 nanoparticles with a size of 10–20 nm are uniformly distributed on the fiber surface through covalent tethering, without blocking the pores in the electrospun mats. The attachment of SiO_2 nanoparticles results in a remarkable improvement in the mechanical properties of the nanofibrous mats. IL-based polymer electrolytes can be facilely prepared by immersing SiO_2-on-P(VDF–HFP) nanofibrous mats in $BMIM^+BF_4^-$ and $LiClO_4/BMIM^+BF_4^-$ liquid electrolytes. Significant enhancement of ionic conductivity and lithium transference number is achieved, which is attributed to the enhanced salt dissociation caused by Lewis acid–base interactions of SiO_2 with BF_4^- and ClO_4^-. The electrochromic device using the IL-loaded SiO_2-on-P(VDF–HFP) nanofibrous mats as the electrolyte layer shows an enhanced contrast, as a result of the increased number of free lithium ions. The hybrid mats are also loaded with $LiTFSI/PYR_{14}^+TFSI^-$, and the resulting electrolytes are tested in $Li/LiCoO_2$ cells. The incorporation of SiO_2 improves the lithium transference number and compatibility with the lithium electrode, leading to much enhanced rate capacity and good cycling stability of the cells. We believe that this approach may also be adopted to prepare non-volatile electrolytes for other types of devices, such as supercapacitors and fuel cells. Furthermore, it also paved the way for tethering other types of inorganic nanoparticles onto PVDF-based nanofibers for a wide variety of applications.

Acknowledgements

Rui Zhou thanks Nanyang Technological University, Singapore for providing her Ph.D. scholarship in course of this work. This work was supported by Science and Engineering Research Council of the Agency for Science, Technology and Research (A*Star) and Ministry of National Development, Singapore under Grants 132 176 0013 and 132 176 0011.

Notes and references

1 G. F. Starkulla, S. Klenk, M. Butschies, S. Tussetschläger and S. Laschat, *J. Mater. Chem.*, 2012, **22**, 21987–21997.
2 E. T. Fox, J. E. F. Weaver and W. A. Henderson, *J. Phys. Chem. C*, 2012, **116**, 5271–5275.
3 M. Díaz, A. Ortiz and I. Ortiz, *J. Membr. Sci.*, 2014, **469**, 379–396.
4 T. Vogl, S. Menne, R.-S. Kuehnel and A. Balducci, *J. Mater. Chem. A*, 2014, **2**, 8258–8265.
5 N. Shirshova, A. Bismarck, S. Carreyette, Q. P. V. Fontana, E. S. Greenhalgh, P. Jacobsson, P. Johansson, M. J. Marczewski, G. Kalinka, A. R. J. Kucernak, J. Scheers, M. S. P. Shaffer, J. H. G. Steinke and M. Wienrich, *J. Mater. Chem. A*, 2013, **1**, 15300–15309.
6 R. Zhou, W. S. Liu, J. H. Kong, D. Zhou, G. Q. Ding, Y. W. Leong, P. K. Pallathadka and X. H. Lu, *Polymer*, 2014, **55**, 1520–1526.
7 S. Desai, R. L. Shepherd, P. C. Innis, P. Murphy, C. Hall, R. Fabretto and G. G. Wallace, *Electrochim. Acta*, 2011, **56**, 4408–4413.
8 Y. S. Ye, J. Rick and B. J. Hwang, *J. Mater. Chem. A*, 2013, **1**, 2719–2743.
9 D. Zhou, R. Zhou, C. Chen, W. A. Yee, J. Kong, G. Ding and X. Lu, *J. Phys. Chem. B*, 2013, **117**, 7783–7789.
10 N. Shirshova, P. Johansson, M. J. Marczewski, E. Kot, D. Ensling, A. Bismarck and J. H. G. Steinke, *J. Mater. Chem. A*, 2013, **1**, 9612–9619.
11 L. C. Bradley and M. Gupta, *Langmuir*, 2012, **28**, 10276–10280.
12 J. M. Virgili, A. J. Nedoma, R. A. Segalman and N. P. Balsara, *Macromolecules*, 2010, **43**, 3750–3756.
13 J. M. Virgili, A. Hexemer, J. A. Pople, N. P. Balsara and R. A. Segalman, *Macromolecules*, 2009, **42**, 4604–4613.
14 Y. Z. Liang, S. C. Cheng, J. M. Zhao, C. H. Zhang, S. Y. Sun, N. T. Zhou, Y. P. Qiu and X. W. Zhang, *J. Power Sources*, 2013, **240**, 204–211.
15 F. M. Vitucci, D. Manzo, M. A. Navarra, O. Palumbo, F. Trequattrini, S. Panero, P. Bruni, F. Croce and A. Paolone, *J. Phys. Chem. C*, 2014, **118**, 5749–5755.
16 P. Raghavan, J.-W. Choi, J.-H. Ahn, G. Cheruvally, G. S. Chauhan, H.-J. Ahn and C. Nah, *J. Power Sources*, 2008, **184**, 437–443.
17 W. W. Cui, D. Y. Tang and Z. L. Gong, *J. Power Sources*, 2013, **223**, 206–213.
18 R. Zhou, K. P. Pramoda, W. Liu, D. Zhou, G. Ding, C. He, Y. W. Leong and X. Lu, *Electrochim. Acta*, 2014, **146**, 224–230.

19 N. Byrne, J. Efthimiadis, D. R. MacFarlane and M. Forsyth, *J. Mater. Chem.*, 2004, **14**, 127–133.

20 K. L. Mathews, A. M. Budgin, S. Beeram, A. T. Joenathan, B. D. Stein, U. Werner-Zwanziger, M. Pink, L. A. Baker, W. E. Mahmoud, J. P. Carini and L. M. Bronstein, *J. Mater. Chem. A*, 2013, **1**, 1108–1116.

21 M. Marcinek, A. Bac, P. Lipka, A. Zalewska, G. Zukowska, R. Borkowska and W. Wieczorek, *J. Phys. Chem. B*, 2000, **104**, 11088–11093.

22 F. Croce, R. Curini, A. Martinelli, L. Persi, F. Ronci, B. Scrosati and R. Caminiti, *J. Phys. Chem. B*, 1999, **103**, 10632–10638.

23 L. Li, Z. Wu, S. Yuan and X.-B. Zhang, *Energy Environ. Sci.*, 2014, **7**, 2101–2122.

24 S. W. Choi, S. M. Jo, W. S. Lee and Y. R. Kim, *Adv. Mater.*, 2003, **15**, 2027–2032.

25 M. Yanilmaz, Y. Lu, M. Dirican, K. Fu and X. Zhang, *J. Membr. Sci.*, 2014, **456**, 57–65.

26 S. X. Xiong, S. L. Phua, B. S. Dunn, J. Ma and X. H. Lu, *Chem. Mater.*, 2010, **22**, 255–260.

27 S. Xiong, P. Jia, K. Y. Mya, J. Ma, F. Boey and X. Lu, *Electrochim. Acta*, 2008, **53**, 3523–3530.

28 W. W. Schmiegel, *Angew. Makromol. Chem.*, 1979, **76–77**, 39–65.

29 X.-J. Zhang, G.-S. Wang, W.-Q. Cao, Y.-Z. Wei, M.-S. Cao and L. Guo, *RSC Adv.*, 2014, **4**, 19594–19601.

30 N. Li, C. Xiao, S. An and X. Hu, *Desalination*, 2010, **250**, 530–537.

31 V. R. Koganti, S. Das and S. E. Rankin, *J. Phys. Chem. C*, 2014, **118**, 19450–19461.

32 Y.-J. Kim, C. H. Ahn and M. O. Choi, *Eur. Polym. J.*, 2010, **46**, 1957–1965.

33 W. Li, Y. Xing, Y. Wu, J. Wang, L. Chen, G. Yang and B. Tang, *Electrochim. Acta*, 2015, **151**, 289–296.

34 K. Hanabusa, H. Fukui, M. Suzuki and H. Shirai, *Langmuir*, 2005, **21**, 10383–10390.

35 S. A. M. Noor, P. M. Bayley, M. Forsyth and D. R. MacFarlane, *Electrochim. Acta*, 2013, **91**, 219–226.

36 Q. Zhou, K. Fitzgerald, P. D. Boyle and W. A. Henderson, *Chem. Mater.*, 2010, **22**, 1203–1208.

37 S. Schantz, L. M. Torell and J. R. Stevens, *J. Chem. Phys.*, 1991, **94**, 6862–6867.

38 V. K. Thakur, G. Ding, J. Ma, P. S. Lee and X. Lu, *Adv. Mater.*, 2012, **24**, 4071–4096.

39 Y. Y. Lu, S. S. Moganty, J. L. Schaefer and L. A. Archer, *J. Mater. Chem.*, 2012, **22**, 4066–4072.

40 C. Xu, B. Sun, T. Gustafsson, K. Edström, D. Brandell and M. Hahlin, *J. Mater. Chem. A*, 2014, **2**, 7256–7264.

41 X.-L. Huang, D. Xu, S. Yuan, D.-L. Ma, S. Wang, H.-Y. Zheng and X.-B. Zhang, *Adv. Mater.*, 2014, **26**, 7264–7270.

42 S. Yuan, X.-L. Huang, D.-L. Ma, H.-G. Wang, F.-Z. Meng and X.-B. Zhang, *Adv. Mater.*, 2014, **26**, 2273–2279.